Supplementary Information for

Bulk nanostructured intermetallic alloys enable superb strength-ductility synergy and thermal stability

Lijun Jing[1,2], Biao Xu[3,4], Yixiang Wang[1], Zhankun Zhao[1], Jian Cui[1], Bowen Han[1], Qiaozhen Shen[1], Guanyu Chen[1], Peter K. Liaw[5], Tao Yang[2,6,*], Yilu Zhao[1, **]

[1] *School of Materials Science and Engineering, Harbin Institute of Technology (Shenzhen), Shenzhen 518055, China*

[2] *Department of Materials Science and Engineering, City University of Hong Kong, Hong Kong, China*

[3] *School of Physics and Electronics, Hunan University, Changsha 410082, China*

[4] *Centre for Advanced Nuclear Safety and Sustainable Development, City University of Hong Kong, Hong Kong 999077, China*

[5] *Department of Materials Science and Engineering, University of Tennessee, Knoxville, USA*

[6] *Centre for Advanced Structural Materials, City University of Hong Kong, Hong Kong 999077, China*

* *Corresponding authors: taoyang6-c@my.cityu.edu.hk (Tao Yang); zhaoyilu@hit.edu.cn (Yilu Zhao)*

Contents

Supplementary note

Calculation of back stress and effective stress

A magnified hysteresis loop (**Supplementary Fig. 11**) illustrates the determination of the σ_b and σ_{eff} according to the following equations[1]:

$$\sigma_b = \frac{\sigma_u + \sigma_r}{2} \tag{1}$$

$$\sigma_{eff} = \sigma_f - \sigma_b \tag{2}$$

where σ_f represents the flow stress, σ_u denotes the unloading yield stress and σ_r signifies the reloading yield stress.

Supplementary Figures

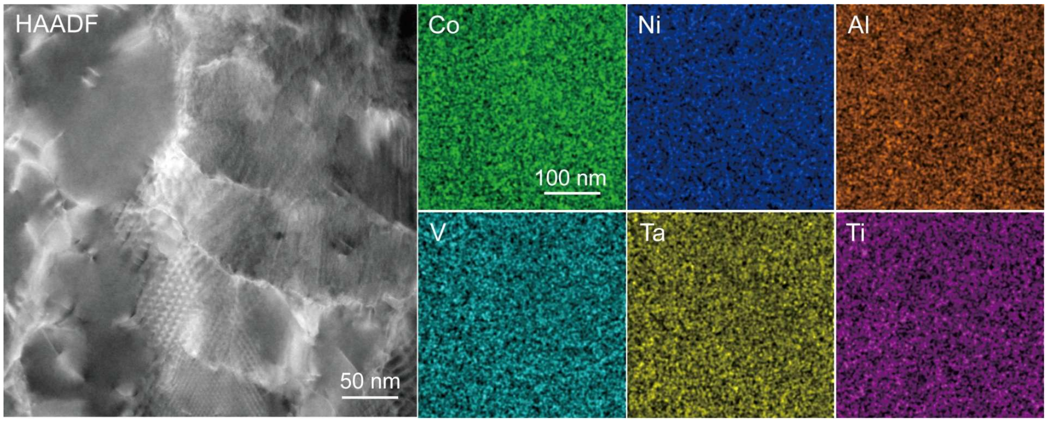

Supplementary Fig. 1. Low-angle-misoriented subgrains of the BBN CCIMA sample. HAADF image and corresponding EDS mapping, showing an absence of elemental segregation on the LADBs separating the subgrains.

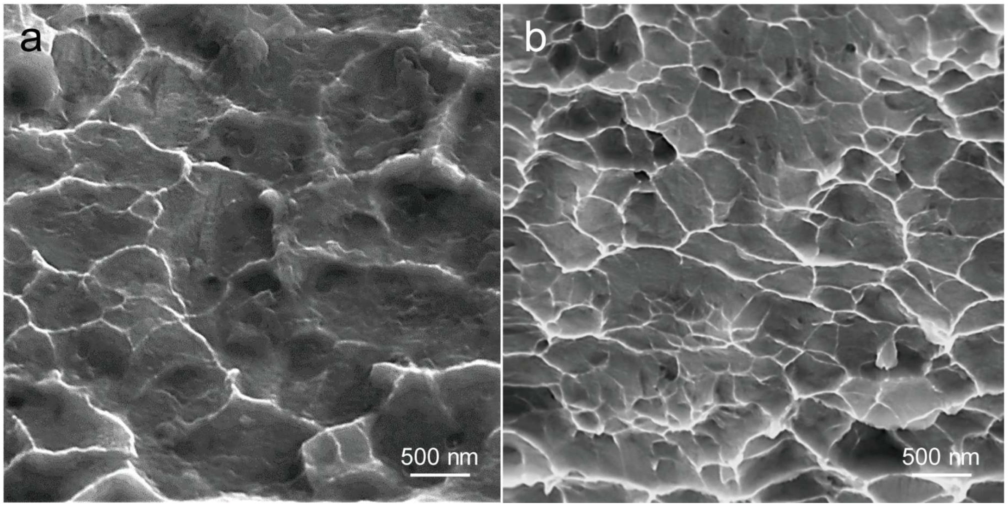

Supplementary Fig. 2. Fracture morphologies of the BBN CCIMA. a, RT **b,** LNT, both showing ductile fracture feature.

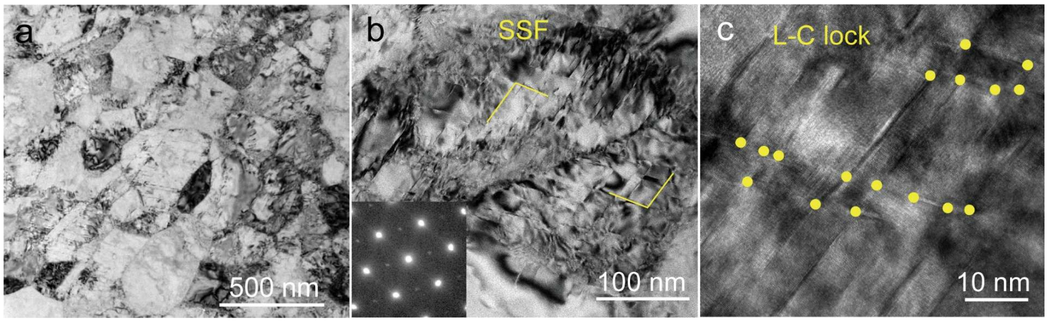

Supplementary Fig. 3. Deformation mechanism in the UFG region of the BBN CCIMA sample under RT. a, Low-magnified BF-TEM image, showing high-density dislocations. **b-c,** High-magnified BF-TEM and HRTEM images, showing two sets of intersecting SSFs and resulting L-C locks in UFGs with sizes less than 300 nm. The inset shows the corresponding SAED pattern.

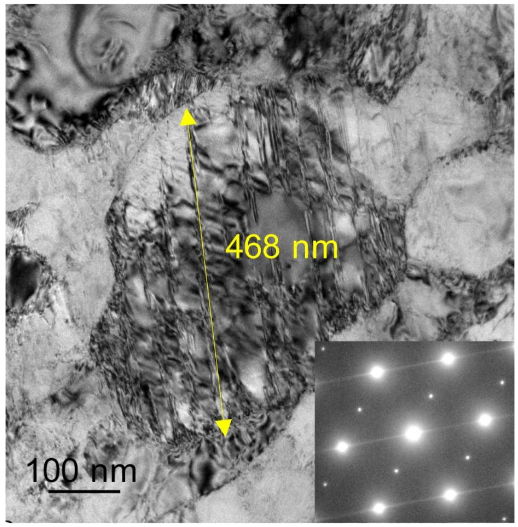

Supplementary Fig. 4. Deformation mechanism in the UFG region with the grain sizes of 400-500 nm of the BBN CCIMA sample under LNT. BF-TEM image and the corresponding SAED pattern, showing SSFs.

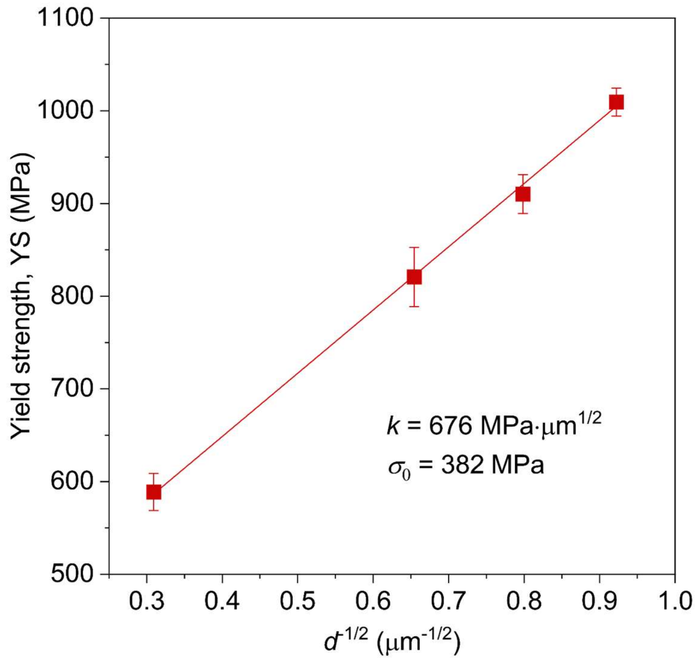

Supplementary Fig. 5. Hall-Petch relation of the present CCIMA.

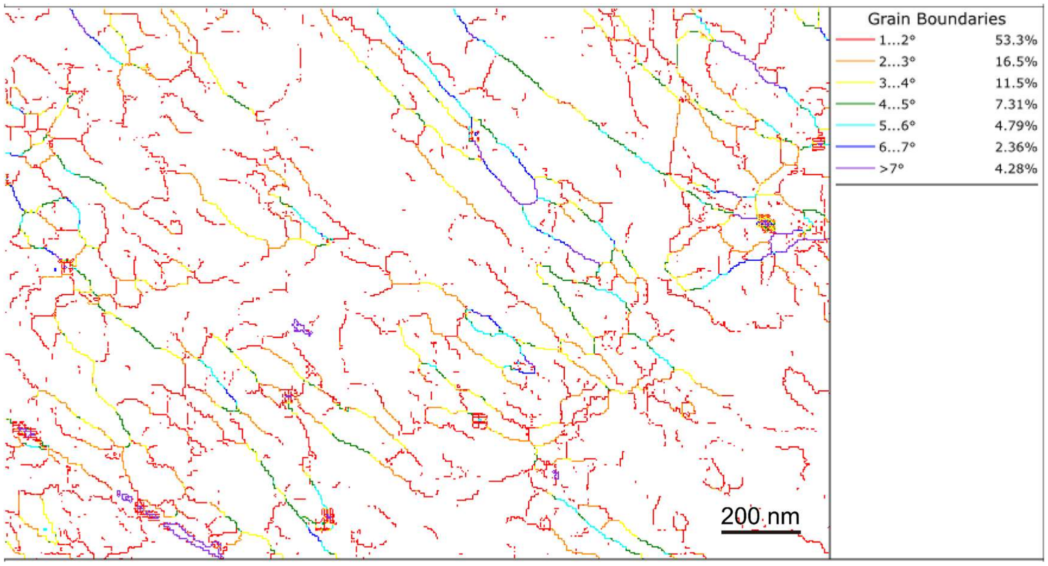

Supplementary Fig. 6. TKD characterization of the NSGs of the as-prepared BBN CCIMA, showing average misorientation of the LADBs of ~ 1.5°.

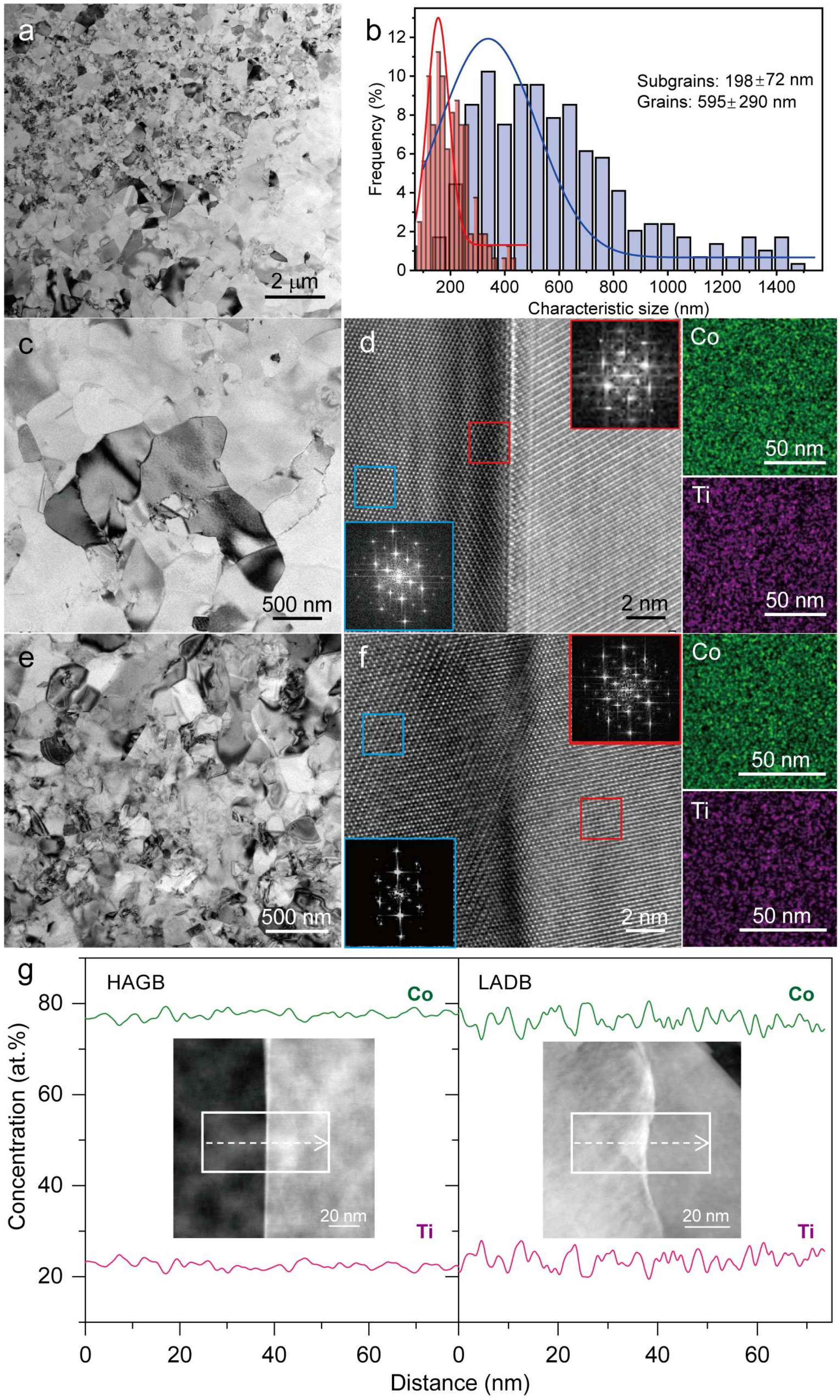
a
2 μm
b
Subgrains: 198±72 nm
Grains: 595±290 nm
Frequency (%)
Characteristic size (nm)
c
500 nm
d
2 nm
Co
50 nm
Ti
50 nm
e
500 nm
f
2 nm
Co
50 nm
Ti
50 nm
g
HAGB
LADB
Co
Ti
20 nm
20 nm
Concentration (at.%)
Distance (nm)

Supplementary Fig. 7. Microstructures of the as-prepared chemically simple $Co_{76}Ti_{24}$(B) sample. a, Low-magnified BF-TEM image. **b,** Statistical characteristic size distributions of grains and subgrains, showing a bimodal feature. **c-d,** UFGs. **e-f,** NSGs. **c, e,** High-magnified BF-TEM images. **d, f,** HRTEM image of an edge-on HAGB and LADB. The two insets are the FFT images, corresponding to the cyan and red squares. The right side is the EDS mapping. **g,** Quantitative compositional profiles across the HAGB and LADB, showing absence of elemental segregation.

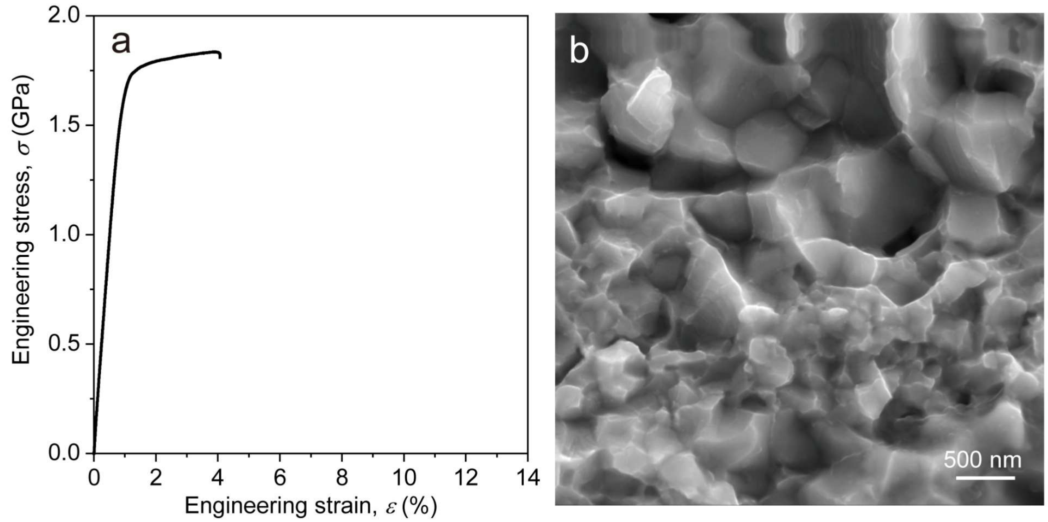

Supplementary Fig. 8. Tensile property of the chemically simple $Co_{76}Ti_{24}$(B) sample under RT. a, Tensile engineering stress-strain curve showing limited ductility. **b,** Fracture morphologies, showing brittle intergranular fracture feature.

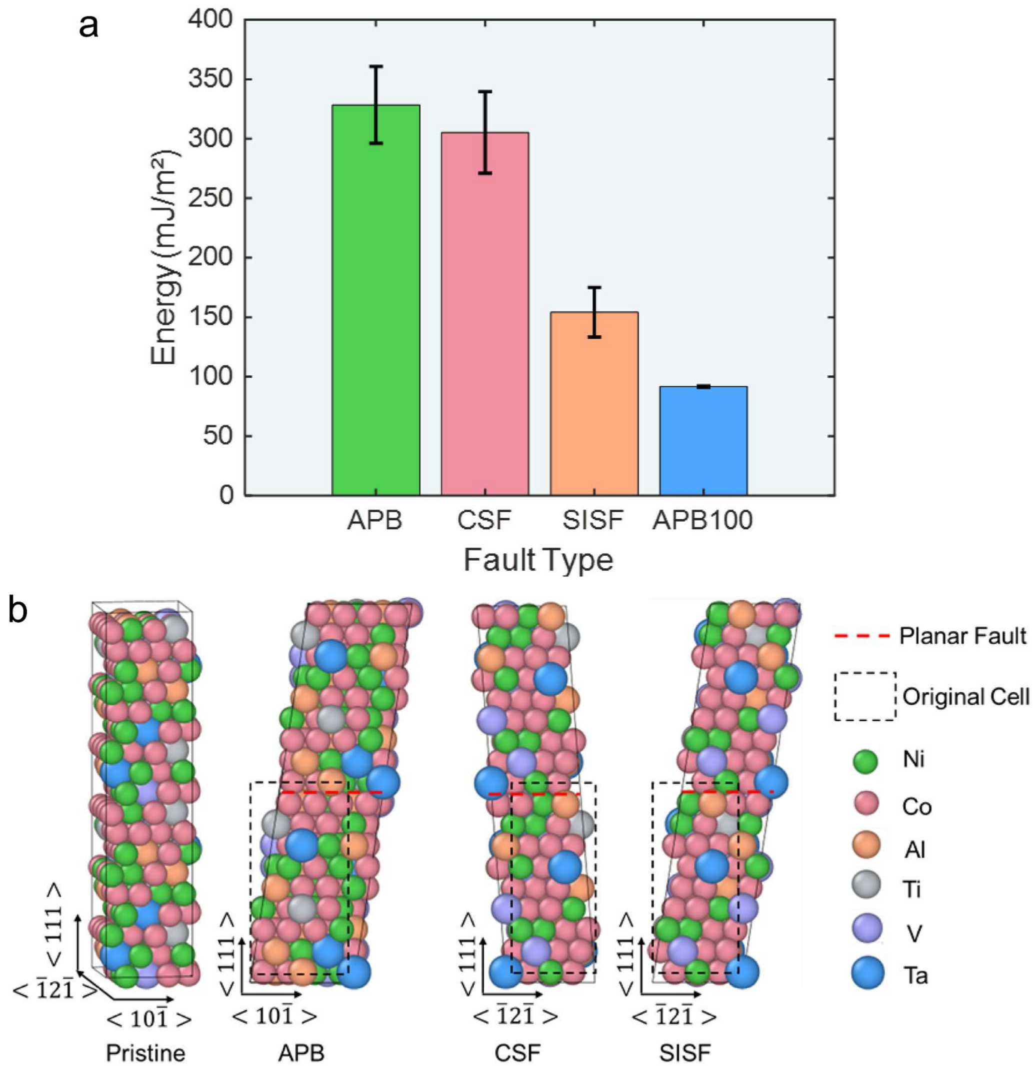

Supplementary Fig. 9. DFT calculations of planar fault energies. a, Calculated planar fault energies for APB, CSF, SISF (along the <111> direction), and APB_{100} (along the <100> direction) in the Co-Ni-Al-Ti-V-Ta alloy. **b,** Cell structure model used for calculating planar fault energies along the <111> direction.

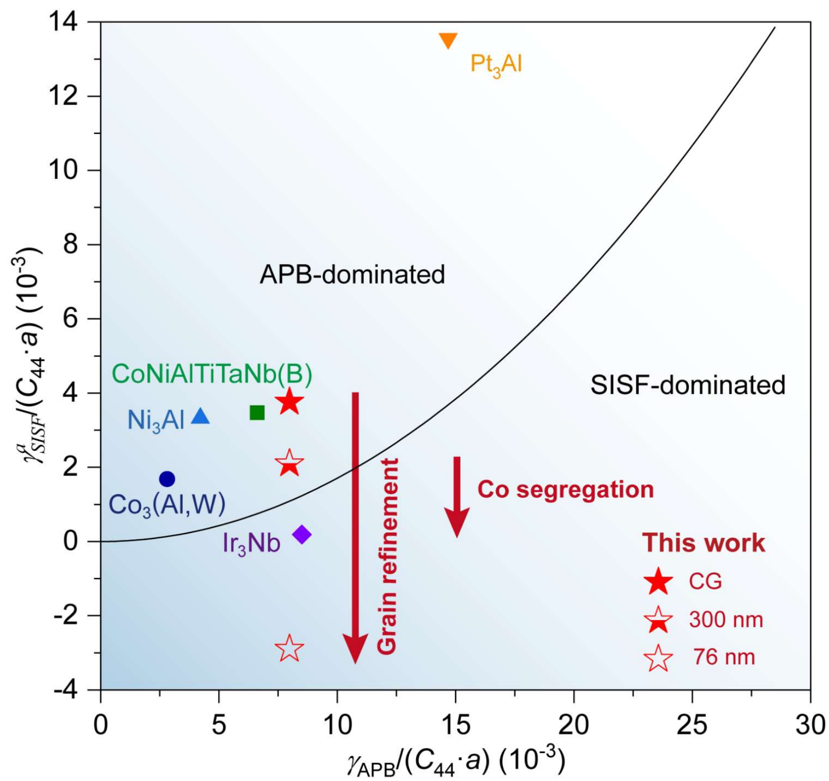

Supplementary Fig. 10. Boundary map for the APB-dominated and the SISF-dominated mechanisms in L1$_2$-type IMAs. The dependence of the γ^{a}_{SISF} on grain size and the Co-segregation-induced reduction in local γ_{SISF} for the present alloy are taken into account. For simplification, only the results corresponding to screw dislocations are presented. Results related to edge dislocations showcase a similar dependence on grain size, but with a higher γ^{a}_{SISF}. The data of Ni_3Al, $Co_3(Al,W)$, Ir_3Nb and Pt_3Al are from the reference[2], while the data of CoNiAlTiTaNb(B) is from the reference[3].

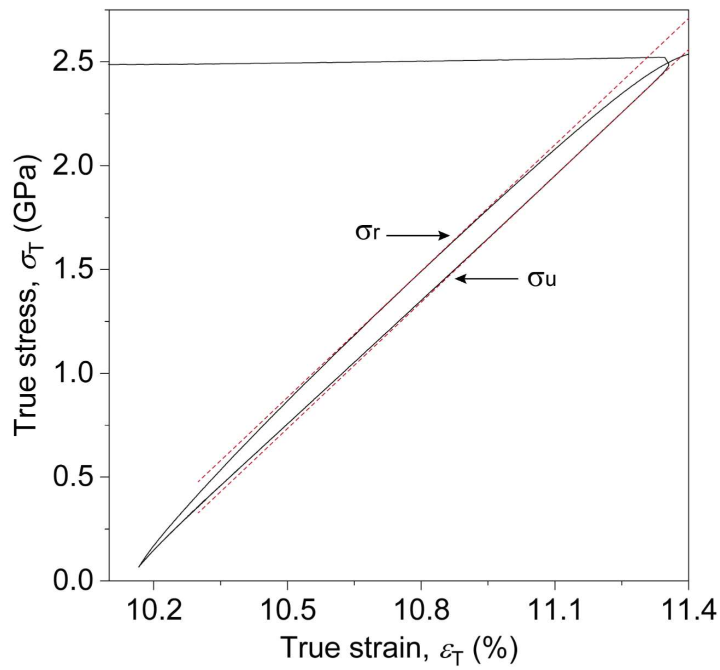

Supplementary Fig. 11. Illustration of the determination of σ_b and σ_{eff}, depicted in a magnified unloading-reloading branch of the hysteresis loop of the BBN CCIMA sample. Symbols: σ_u -unloading yield stress, σ_r -reloading yield stress.

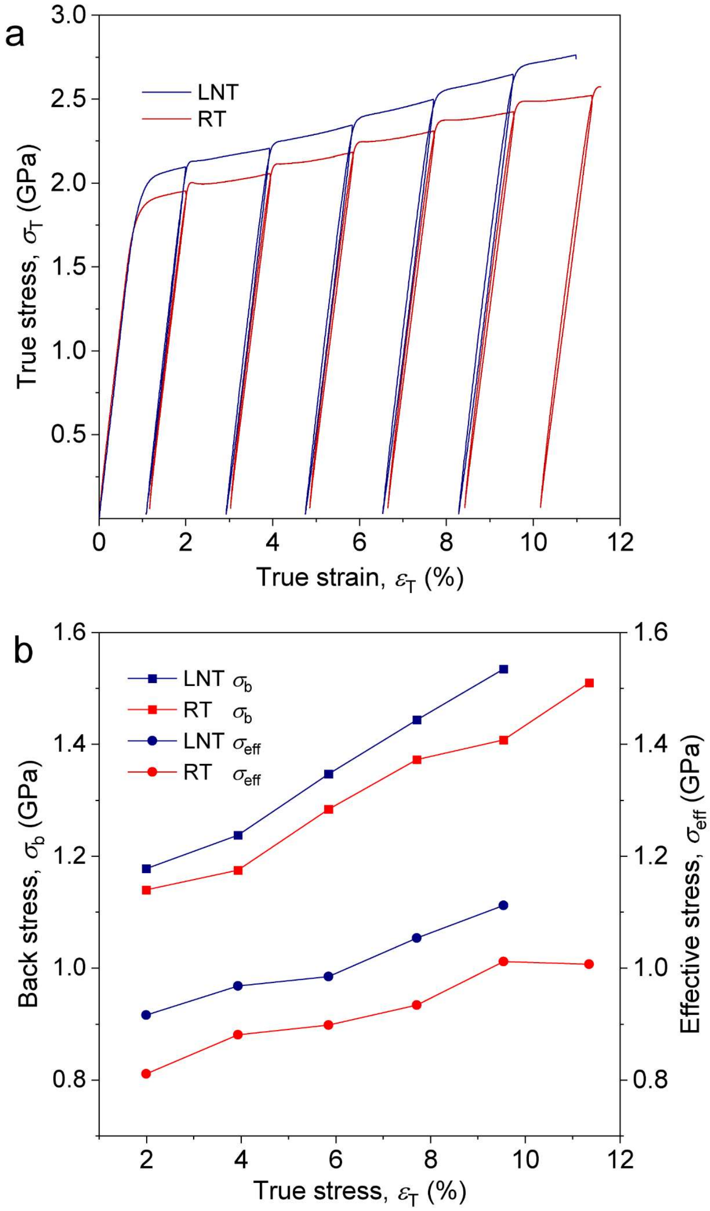

Supplementary Fig. 12. Back stress and effective stress of the BBN CCIMA. a, Evolution of the true stress-strain hysteresis loop during the loading-unloading-reloading cycles. **b,** Evolutions of σ_b and σ_{eff} with ε_T.

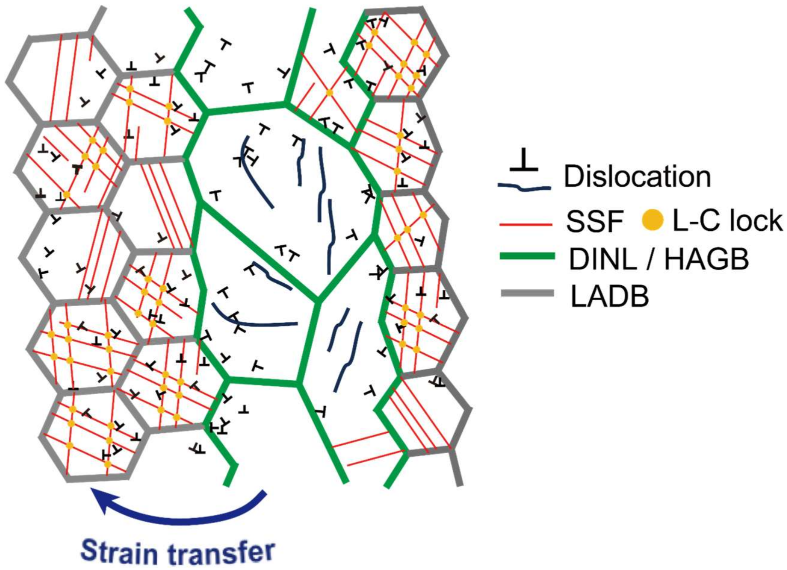

Supplementary Fig. 13. Schematic illustration of the multiple deformation mechanisms of the BBN CCIMA.

Supplementary Table 1. Composition, grain size and tensile properties of various alloys in Figs. 2c, d.

Composition	Preparation method	Sample dimension (mm³)	Grain size (nm)	YS (MPa)	UTS (MPa)	UTS-YS (MPa)	δu (%)	Ref.
$(Co_{47}Ni_{30}Al_{10}V_5Ta_4Ti_4)_{99}B_1$	CR + Annealing	12.5×2×0.4	311/76	1833	2250	420	14	RT
			311/76	2190	2654	464	13	LNT
$Co_{76}Ti_{24}$(B)			595/198	1661	1831	170	4	RT
Ni	ED	1.72×0.25×0.2	21	1600	2040	440	4	4
		6×2.5×0.2	21	1430	1820	390	2.6	4
	PED	4.5×2.2×0.13	29	839	1266	427	4	5
Cu	LNT+RT BM	3×(1-2)×(0.15-0.3)	54	688	760	72	2.6	6
	ECAP	3×2	230	500	550	50	2.2	7
	IGC + WC		16	360	480	120	1.6	7
	HPT + CR	10×1×0.15	180	420	470	50	2.2	8
Pd	IGC + WC	3×2	36	550	600	50	2.6	7
			47	660	685	25	4	7
CoCu	ED	7×2×0.01	110	1420	1875	455	3.3	9
CoP	PED	15×1.5×0.5	12	1200	1680	480	1.1	10
$CuAl_{11}$	ECAP	8×2×1	200	619	780	161	3.7	11
Cu-1Nb	BM	2×1×0.4	18	1035	1308	273	8.7	12
Cu-10Zn	BM + HPT	2×1	110	580	680	100	3.8	13
Cu-30Zn			28	930	1220	290	2.8	13
Cu-30Zn			26	730	850	120	1.8	13
$CuAl_{12.1}Zn_{4.1}$	BM	2×1×0.4	22	1067	1200	133	6.5	12

7075 Al alloy	HPT	2×1×0.5	26	977	1050	73	2.6	[14]
	Cryogenic rolling	10×2×0.15	100	550	580	30	3.3	[15]
			100	615	670	55	7.4	[15]
CrCoNi	CR + Annealing	10×2×0.6	230	1400	1500	100	1.7	[16]
CrMnFeCoNi		8×2×1	27	900	929	29	5.7	[17]
5083 Al alloy	Milling + Compact + Extrusion	12×4×2	200/1000	608	711	103	0.9	[18]
6063 Al alloy		9×2	80-1400/1800-4100	188	266	78	6	[19]

Note: The following abbreviations are used: CR: cold rolling; ED: electrodeposition; PED: pulsed electrodeposition; LNT: liquid nitrogen temperature; RT: room temperature; BM: ball milling; ECAP: equal channel angular pressing; IGC: Insert-gas condensation; WC: warm compaction; HPT: high-pressure torsion.

Supplementary References

1 Yang, M., Pan, Y., Yuan, F., Zhu, Y. & Wu, X. Back stress strengthening and strain hardening in gradient structure. *Mater Res Lett* **4**, 145-151 (2016).

2 Okamoto, N. L., Takemoto, S., Chen, Z. M. T., Yamaguchi, M. & Inui, H. FCC metal-like deformation behaviour of Ir_3Nb with the $L1_2$ structure. *International Journal of Plasticity* **97**, 145-158 (2017).

3 Xiao, B. *et al.* Ultrahigh intermediate-temperature strength and good tensile plasticity in chemically complex intermetallic alloys via lamellar architectures. *Acta Materialia* **262**, 119459 (2024).

4 Dalla Torre, F., Van Swygenhoven, H. & Victoria, M. Nanocrystalline electrodeposited Ni: microstructure and tensile properties. *Acta Materialia* **50**, 3957-3970 (2002).

5 Wang, Y. M. *et al.* Achieving large uniform tensile ductility in nanocrystalline metals. *Physical Review Letters* **105** (2010).

6 Cheng, S. *et al.* Tensile properties of in situ consolidated nanocrystalline Cu. *Acta Materialia* **53**, 1521-1533 (2005).

7 Sanders, P. G., Eastman, J. A. & Weertman, J. R. Elastic and tensile behavior of nanocrystalline copper and palladium. *Acta Materialia* **45**, 4019-4025 (1997).

8 Zhao, Y. H., Zhu, Y. T., Liao, X. Z., Horita, Z. & Langdon, T. G. Tailoring stacking fault energy for high ductility and high strength in ultrafine grained Cu and its alloy. *Applied Physics Letters* **89** (2006).

9 Nakamoto, Y., Yuasa, M., Chen, Y., Kusuda, H. & Mabuchi, M. Mechanical properties of a nanocrystalline Co–Cu alloy with a high-density fine nanoscale lamellar structure.

Scripta Materialia **58**, 731-734 (2008).

10 Fan, G. J., Fu, L. F., Choo, H., Liaw, P. K. & Browning, N. D. Uniaxial tensile plastic deformation and grain growth of bulk nanocrystalline alloys. *Acta Materialia* **54**, 4781-4792 (2006).

11 An, X. H., Wu, S. D., Wang, Z. G. & Zhang, Z. F. Enhanced cyclic deformation responses of ultrafine-grained Cu and nanocrystalline Cu–Al alloys. *Acta Materialia* **74**, 200-214 (2014).

12 Youssef, K., Sakaliyska, M., Bahmanpour, H., Scattergood, R. & Koch, C. Effect of stacking fault energy on mechanical behavior of bulk nanocrystalline Cu and Cu alloys. *Acta Materialia* **59**, 5758-5764 (2011).

13 Bahmanpour, H. *et al.* Deformation twins and related softening behavior in nanocrystalline Cu–30% Zn alloy. *Acta Materialia* **60**, 3340-3349 (2012).

14 Liddicoat, P. V. *et al.* Nanostructural hierarchy increases the strength of aluminium alloys. *Nature Communications* **1**, 63 (2010).

15 Zhao, Y. H., Liao, X. Z., Cheng, S., Ma, E. & Zhu, Y. T. Simultaneously increasing the ductility and strength of nanostructured alloys. *Advanced Materials* **18**, 2280-2283 (2006).

16 Guo, F. J. *et al.* The critical grain size for optimal strength–ductility synergy in CrCoNi medium entropy alloy. *Scripta Materialia* **218**, 114808 (2022).

17 Wang, Y. *et al.* Activating dispersed strain bands in tensioned nanostructure layer for high ductility: The effects of microstructure inhomogeneity. *International Journal of Plasticity* **149**, 103159 (2022).

18 Han, B. Q., Lavernia, E. J., Lee, Z., Nutt, S. & Witkin, D. Deformation behavior of bimodal

nanostructured 5083 Al alloys. *Metallurgical and Materials Transactions A* **36**, 957-965 (2005).

19 Oskooie, M. S. & Asgharzadeh, H. in *6th International Conference on Nanomaterials by Severe Plastic Deformation (NanoSPD)*. (2014).